LETTER

https://doi.org/10.1038/s41586-019-1304-2

Spin–orbit–driven band inversion in bilayer graphene by the van der Waals proximity effect

J. O. Island[1], X. Cui[1], C. Lewandowski[2], J. Y. Khoo[2], E. M. Spanton[1], H. Zhou[1], D. Rhodes[3], J. C. Hone[3], T. Taniguchi[4], K. Watanabe[4], L. S. Levitov[2], M. P. Zaletel[5] & A. F. Young[1]*

Spin–orbit coupling (SOC) is the key to realizing time-reversal-invariant topological phases of matter[1,2]. SOC was predicted by Kane and Mele[3] to stabilize a quantum spin Hall insulator; however, the weak intrinsic SOC in monolayer graphene[4–7] has precluded experimental observation in this material. Here we exploit a layer-selective proximity effect—achieved via a van der Waals contact with a semiconducting transition-metal dichalcogenide[8–21]—to engineer Kane–Mele SOC in ultra clean bilayer graphene. Using high-resolution capacitance measurements to probe the bulk electronic compressibility, we find that SOC leads to the formation of a distinct, incompressible, gapped phase at charge neutrality. The experimental data agree quantitatively with a simple theoretical model in which the new phase results from SOC-driven band inversion. In contrast to Kane–Mele SOC in monolayer graphene, the inverted phase is not expected to be a time-reversal-invariant topological insulator, despite being separated from conventional band insulators by electric-field-tuned phase transitions where crystal symmetry mandates that the bulk gap must close[22]. Our electrical transport measurements reveal that the inverted phase has a conductivity of approximately e^2/h (where e is the electron charge and h Planck's constant), which is suppressed by exceptionally small in-plane magnetic fields. The high conductivity and anomalous magnetoresistance are consistent with theoretical models that predict helical edge states within the inverted phase that are protected from backscattering by an emergent spin symmetry that remains robust even for large Rashba SOC. Our results pave the way for proximity engineering of strong topological insulators as well as correlated quantum phases in the strong spin–orbit regime in graphene heterostructures.

Depending on microscopic symmetry, SOC in graphene can take several forms, leading in turn to different electronic states at charge neutrality. In the absence of SOC, the low-energy electronic structure of monolayer graphene is described by Dirac equations in two inequivalent valleys centred at the two momenta K and K′ of the hexagonal Brillouin zone. SOC, along with other perturbations that break the equivalence of the two valleys or two carbon sublattices, can be written with the aid of three sets of Pauli matrices, $\hat{\sigma}_i$, $\hat{\tau}_i$ and $\hat{s}_i$, which operate on the space of the carbon sublattices within the graphene unit cell, the K and K′ valleys, and the physical electron spin, respectively. If the full symmetry of the graphene crystal is preserved, the only symmetry-allowed SOC term at low energies is the Kane–Mele (KM) term[3], $H_{\mathrm{KM}} = \frac{\lambda_{\mathrm{KM}}}{2}\sigma_z\tau_z s_z$, where λ_{KM} is the Kane–Mele SOC strength. However, additional terms can arise when experimental substrates break lattice symmetries; these include the Rashba SOC, $H_{\mathrm{R}} = \lambda_{\mathrm{R}}(\sigma_x\tau_z s_y - \sigma_y s_x)$, and the so-called Ising SOC, $H_{\mathrm{I}} = \lambda_{\mathrm{I}}\tau_z s_z$. In monolayer graphene, only the intrinsic λ_{KM} term leads to a topological phase[3,12]. Moreover, this topological phase requires[3] $\lambda_{\mathrm{R}} < \lambda_{\mathrm{KM}}$, which is a physically unrealistic[4–6] scenario given the measured[7] value $\lambda_{\mathrm{KM}} \approx 40\ \mu\mathrm{eV}$.

Proximity effects between two-dimensional crystals provide a tool for engineering electronic structures that do not occur naturally within a single material. First-principles calculations indicate[8,9] that heterostructures of graphene and transition-metal dichalcogenide (TMD) semiconductors such as tungsten diselenide (WSe_2) may endow graphene electrons with a SOC strength of several millielectronvolts—two orders of magnitude larger than the intrinsic Kane–Mele SOC[7] and sufficient, in principle, to enable observation of new topological phases[23]. Numerous experimental efforts have reported signatures of enhanced SOC in graphene–TMD heterostructures. However, most rely on measurements of either spin relaxation[17–21] or weak antilocalization[10–16], both of which are sensitive to disorder and interface quality; this sensitivity affects scattering rates and as a consequence inferred SOC strength. One study[11] of quantum oscillations found evidence for Rashba SOC within graphene band electrons of bilayer graphene (BLG), but neither Ising SOC nor a λ_{KM}-driven topological phase[3] have been reported.

Here we explore the effects of proximity-induced SOC in van der Waals heterostructures built around BLG–tungsten diselenide (WSe_2) interfaces (see Methods). In contrast to monolayer graphene, the electronic spectrum of BLG features a quadratic band touching at charge neutrality. An applied perpendicular electric displacement field, D, drives the system to a layer-polarized band insulator in which wavefunctions are strongly polarized on the low-energy layer, making BLG an ideal tool for probing short-range van der Waals proximity effects. To access subtle features within the electronic structure, we use hexagonal boron nitride (hBN) gate dielectrics[24] and single-crystal graphite top- and bottom-gate electrodes, which reduce charge inhomogeneity[25] while simultaneously allowing independent control over the charge carrier density, n, and D (see Fig. 1a). We measure the penetration field capacitance, $C_{\mathrm{P}} = c^2/(2c + \partial n/\partial\mu)$, where c is the geometric capacitance and μ is the chemical potential. It is inversely related to the bulk electronic compressibility, $\partial n/\partial\mu$, so that electronic gaps manifest as C_{P} maxima. Figure 1b shows C_{P} as a function of n and D measured in a BLG flake symmetrically encapsulated in WSe_2. The most prominent features of the data are incompressible states at $n \approx 0$ associated with layer-polarized band insulators, which deepen as $|D|$ increases and are characteristic of BLG. However, WSe_2 encapsulation also produces features associated with proximity-induced SOC. First, four weak C_{P} minima appear at finite n (indicated by arrows in Fig. 1b), whose positions depend strongly on D. Second, an additional incompressible phase is observed at charge neutrality near $D = 0$, separated from the band insulators by points of high compressibility. We observe the incompressible state in two devices, S1 and S2, which are symmetrically encapsulated in WSe_2, but it does not appear in either hBN-encapsulated device C1 or in devices A1 and A2 that are asymmetrically encapsulated in hBN and WSe_2 (Fig. 1 and Extended Data Fig. 3; see Methods for device names and details).

[1]Department of Physics, University of California, Santa Barbara, CA, USA. [2]Department of Physics, Massachusetts Institute of Technology, Cambridge, MA, USA. [3]Department of Mechanical Engineering, Columbia University, New York, NY, USA. [4]Advanced Materials Laboratory, National Institute for Materials Science, Tsukuba, Japan. [5]Department of Physics, University of California, Berkeley, CA, USA. *e-mail: andrea@physics.ucsb.edu

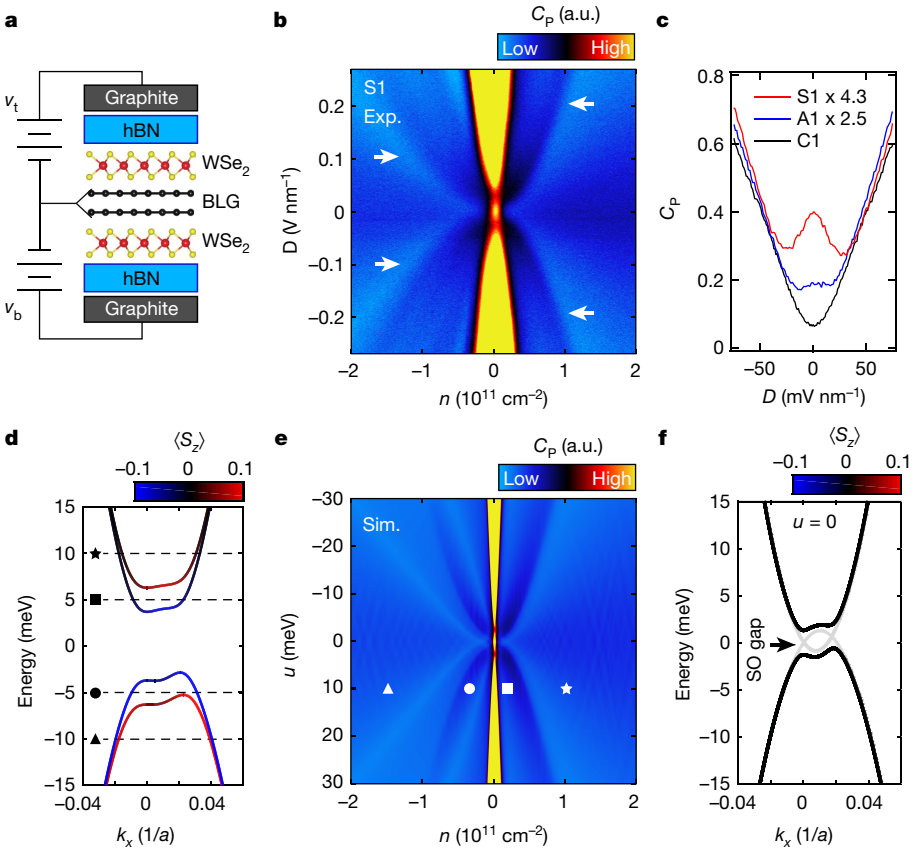

Fig. 1 | Inverted phase in bilayer graphene from proximity-induced SOC. a, Device schematic for a symmetrically WSe_2-encapsulated device. The charge density $n = c_t v_t + c_b v_b$ and perpendicular displacement field $D = (c_t v_t - c_b v_b)/(2\epsilon_0)$ are controlled by the voltages applied to the top and bottom gate ($v_{t(b)}$). **b**, Experimentally (Exp.) measured penetration field capacitance, C_P, as a function of charge density n and displacement field D measured at $B = 0$ and $T \approx 50$ mK in device S1. White arrows indicate compressibility maxima associated with band splitting due to proximity-induced SOC. **c**, C_P experimentally measured at $n = 0$ for a device symmetrically encapsulated with WSe_2 (S1, red), a device asymmetrically encapsulated in hBN and WSe_2 (A1, blue) and a control device fully encapsulated in hBN (C1, black). Only the symmetrically encapsulated device shows an incompressible peak at $D = 0$. The curves for S1 and A1 have been multiplied by a factor for better comparison. **d**, Low-energy bands near the K point of the Brillouin zone for $u = 10$ meV, calculated for a model that includes an Ising SOC of equal magnitude ($\lambda_I = 2.6$ meV) but opposite signs on each layer. **e**, Simulated (Sim.) C_P from the same model. The symbols denote points corresponding to different Fermi levels, as shown in **d**. **f**, Low-energy bands near the K point of the Brillouin zone for $u = 0$, calculated within the same model. The bands are spin degenerate, and a gap (SO gap, arrowed) is visible near zero energy. Light grey bands are calculated in the absence of SOC.

Both experimental features can be captured by a continuum model of BLG (see Supplementary Information) with the sole addition of an Ising SOC term having equal magnitude—but opposite sign—on the two carbon layers (Fig. 1d–f). The opposite sign is consistent with 3D inversion symmetry. Figure 1e shows simulated C_P from this model, in which the only free parameters are the strength of the SOC ($\lambda_I = 2.6$ meV) and the out-of-plane dielectric constant of the BLG ($\epsilon^{\perp}_{BLG} = 4.3$). The latter is used to relate the experimentally measured D to the interlayer potential difference $u = -\frac{d}{\epsilon^{\perp}_{BLG}} D$, which enters the theoretical model (here $d = 0.33$ nm is the BLG interlayer separation). At finite u, Ising SOC splits the normally spin-degenerate conduction and valence bands in BLG (Fig. 1d). The C_P minima arise from the high compressibility associated with the edge of the higher (lower) conduction (valence) band. These band edges appear at finite density after the first bands have already begun filling (Fig. 1d, e).

The C_P maximum observed near $n = 0$, $D = 0$ can be understood by noting that within a two-band model of BLG, layer and carbon sublattice are equivalent[26]. As a result, Ising SOC with opposite signs on opposite layers is equivalent to a single SOC term proportional to σ_z, precisely reproducing the Kane–Mele SOC[3]. The two-band Hamiltonian of WSe_2-encapsulated BLG is thus

$$\hat{H} = \hat{H}_{BLG} + \frac{\lambda_I}{2}\sigma_z s_z \tau_z + \frac{u}{2}\sigma_z \quad (1)$$

where $\hat{H}_{BLG}$ describes BLG in the absence of either SOC or electric fields, and σ_z indexes the two low-energy carbon atoms, or equivalently, the layer.

Within this model, the SOC inverts the bands for $|u| < |\lambda_I|$, opening a gap even at $u = 0$ (Fig. 1f). Owing to the 2π Berry phase of the $\hat{H}_{BLG}$, however, the resulting inverted phase is not predicted to be a strong topological insulator, and the observed incompressible phase near $n = 0$, $D = 0$ is not expected to have edge states protected by time-reversal symmetry. The inverted phase is nevertheless topologically distinct from the high-u band insulators within this model; they differ in the polarization of the insulators' Wannier orbitals, which are pinned to one of three high-symmetry positions within the BLG unit cell[22] (see also Supplementary Information). Theoretically, this distinction guarantees a gap closing between the inverted phase and band insulators, consistent experimentally with the compressible C_P minima.

Proximity-induced SOC arises from overlaps between atomic orbitals, so is only expected to occur for the BLG layer in direct contact with the WSe_2. Figure 2a shows a schematic representation of an asymmetric heterostructure in which WSe_2 is in contact with only the bottom layer. In contrast to the symmetric devices, C_P minima appear in device A1 only for electrons for $D > 0$ and only for holes for $D < 0$ (Fig. 2b). Note that in isolated BLG, all thermodynamic features should respect $D \leftrightarrow -D$ symmetry, suggesting that the asymmetric C_P minima are caused by coupling between the BLG and other elements in the

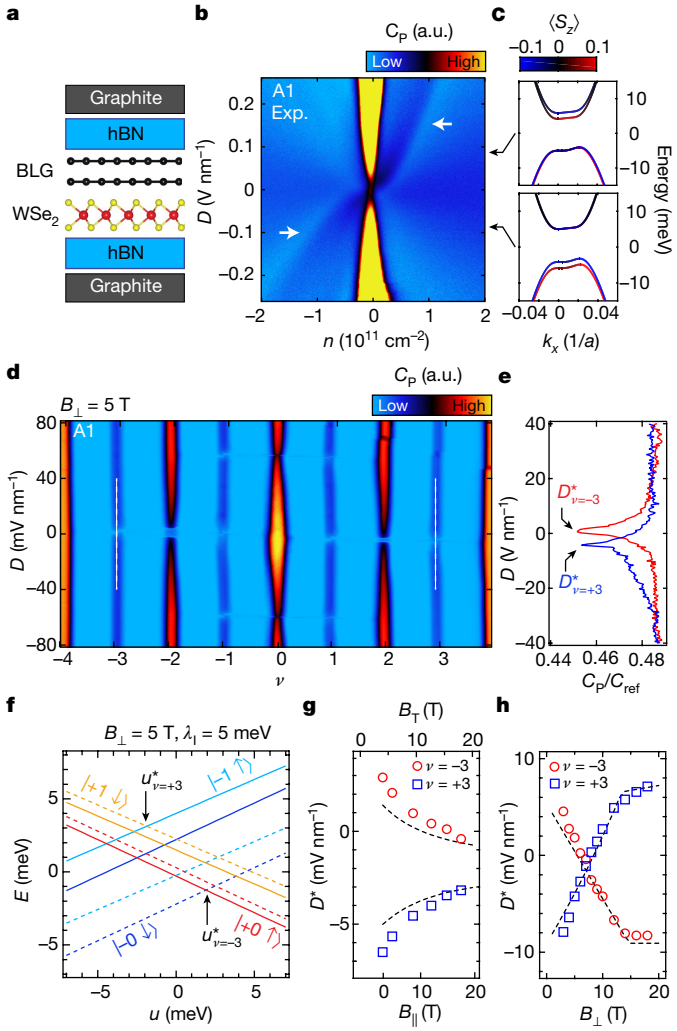

Fig. 2 | Layer-selective spin–orbit proximity effect. a, Schematic of an asymmetrically encapsulated device. **b**, Penetration field capacitance, C_P, as a function of n and D in device A1, experimentally ('Exp.') measured at $B = 0$ and $T \approx 50$ mK. The white arrows indicate compressibility maxima associated with band splitting, which we attribute to proximity-induced SOC. **c**, Low-energy bands near the K point of the Brillouin zone for $u = -10$ meV (top) and $u = 10$ meV (bottom), calculated for a model that includes an Ising SOC of $\lambda_I = 1.7$ meV on the bottom layer. **d**, C_P as a function of $\nu = 2\pi\ell_B^2 n$ (where ℓ_B is the Landau magnetic length) and D for device A1 at $B_\perp = 5$ T. **e**, C_P traces, normalized by the reference capacitance (C_{ref}) on the low temperature amplifier (see Methods), taken at the locations of the white dashed lines in **d** for $\nu = \pm 3$. The minima in C_P correspond to phase transitions that occur at $D^*_{\nu=\pm3}$. **f**, Energy spectrum of the octet LL calculated within a continuum model with $\lambda_I = 5$ meV on the bottom layer. The energy levels are plotted as a function of u for $B_\perp = 5$ T. Solid/dashed lines denote spin projected parallel/antiparallel to the applied $B_\perp$. The indicated $u^*_{\nu=\pm3}$ correspond to the layer transitions for filling or emptying a single level from the octet. Note that for the chosen sign of λ_I, the net spin splitting on the proximity-affected layer is reversed. The kets label states of the zeroth-LL octet involved in the $\nu = \pm 3$ phase transitions with specific valley (+,−), orbital (0,1) and spin (↑,↓) quantum numbers. **g**, Measured $D^*_{\nu=\pm3}$—proportional to $u^*_{\nu=\pm3}$—as a function of the total magnetic field (B_T) for fixed $B_\perp = 4$ T in device A1. The dashed lines are fits to our model (see Supplementary Information) with $\lambda_I = 1.7$ meV on the bottom layer. **h**, Measured $D^*_{\nu=\pm3}$ as a function of $B_\perp$ with $B_\parallel = 0$ in device A1. Dashed lines are fits to the same model as in **g**.

heterostructure. Theoretical simulations (Fig. 2c and Extended Data Fig. 3) confirm that when SOC is induced only on the layer proximate to the WSe_2, the spin splitting is restricted to the conduction (for $D > 0$) or valence (for $D > 0$) band, consistent with the experimental data (see Methods).

The nature of the induced SOC can be precisely validated using the unique properties of BLG in a quantizing perpendicular magnetic field ($B_\perp$), where the zeroth Landau level (LL) is composed of eight degenerate states, spanning $\nu \in (-4, 4)$ as shown in Fig. 2d for device A1. Three features make the octet LL a precision probe of SOC. First, the small scale of the intrinsic splittings between these states allows even few-millielectronvolt-scale SOC[8] to rearrange the LL filling sequence[27]. Second, the octet LL is entirely insensitive to Rashba SOC[27], allowing a direct measurement of the Ising SOC[27]. Last, a broad set of D-field-tuned phase transitions are observed throughout the zero-energy LL, corresponding to transitions between states with differing layer polarizations. The critical displacement field, D^*, required to effect these transitions provides a direct comparison of the energy for LLs on opposite layers (and thus opposite valleys), and can be extracted with high precision (Fig. 2e). Figure 2f shows the single-particle energy spectrum of the octet LL with asymmetric Ising SOC (see Methods). Although the Coulomb interaction changes the order in which these levels fill for $-3 < \nu < 3$, it plays no role in determining which LL fills first ($\nu = -3$) or last ($\nu = 3$)[28]. We thus focus on the observed behaviour of $D^*_{\nu=\pm3}$, which can be simply related to $u^*_{\nu=\pm3}$ calculated from our theoretical model (see Supplementary Information).

The spin structure of the LLs is readily probed by varying the in-plane magnetic field $B_\parallel$ at fixed $B_\perp$, which varies the Zeeman energy but leaves orbital energy scales fixed. In hBN-encapsulated devices, $D^*_{\nu=\pm3}$ is observed to be independent of $B_\parallel$ (Extended Data Fig. 5), consistent with theoretical expectation that the transition occurs between ground states of identical spin. A strikingly different dependence is observed in device A1 (Fig. 2g); now $D^*_{\nu=\pm3}$ is a strong function of $B_\parallel$, indicating that the transition is between ground states with different spin. As shown in the figure, the observed behaviour is quantitatively consistent with our model of Ising SOC on the WSe_2 proximal layer, under the stipulations that λ_I be larger in magnitude than the Zeeman energy (E_Z) due to the applied magnetic field ($\lambda_I > E_Z$) and that the sign of λ_I be chosen to cancel, rather then add, to the $B_\perp$-proportional part of the Zeeman splitting in the affected valley. Under these conditions, the level structure near $\nu = \pm 3$ is inverted, leading to the observed behaviour in $B_\parallel$ (see Extended Data Fig. 5). Moreover, λ_I can now be directly extracted from the dependence[27] of $D^*_{\nu=\pm3}$ on $B_\perp$, in the absence of $B_\parallel$: because the effective Zeeman splitting arising from the SOC is oriented out of plane, an out-of-plane extrinsic Zeeman splitting will precisely cancel it when $2E_Z = 2g\mu_B B_\perp = \lambda_I$, where g is the Landé g-factor and μ_B is the Bohr magneton. Figure 2h shows $D^*_{\nu=\pm3}$ for $B_\parallel = 0$. The two curves cross at $B_\perp \approx 7.4$ T, from which it follows that $\lambda_I = 1.7$ meV (see Extended Data Fig. 9 for a similar analysis of device A2, resulting in $\lambda_I = 2.0$ meV). This value is in reasonable agreement with ab initio calculations[23] predicting $\lambda_I = 1.19$ meV for similar device geometries. The $D^*_{\nu=\pm3}$ transitions are symmetric with respect to the sign of $B_\perp$ because, in the absence of $B_\perp$, the Hamiltonian is time-reversal invariant. Notably, the higher $B_\perp$ phenomenology of our samples suggests that WSe_2 is comparable to[24] hBN as a substrate for high-quality graphene heterostructures, with Coulomb driven states with fractional Hall conductivity observed in compressibility (see Extended Data Figs. 6, 7).

In summary, to account for the bulk thermodynamic measurements of TMD-encapsulated BLG it is necessary to include Ising SOC on the layers proximate to the TMD, with equal and opposite values in the case of symmetric encapsulation. However, our bulk measurements do not quantitatively constrain the Rashba SOC, which has a negligible effect on both the LL structure[27] and the zero magnetic field compressibility[22], and prior experimental estimates[11,13,14,20,29] for λ_R range between 0 and 15 meV. Despite its small influence on the bulk, Rashba SOC may play a critical role in the edge state spectrum of our BLG Hamiltonian, equation (1). For $\lambda_R = 0$, s_z is conserved, and the edge is predicted[22,23] to host two pairs of counter-propagating, spin filtered modes with a quantized conductance (and spin Hall effect) of $4\frac{e^2}{h}$. When $\lambda_R \neq 0$, however, s_z symmetry is weakly broken and backscattering is expected.

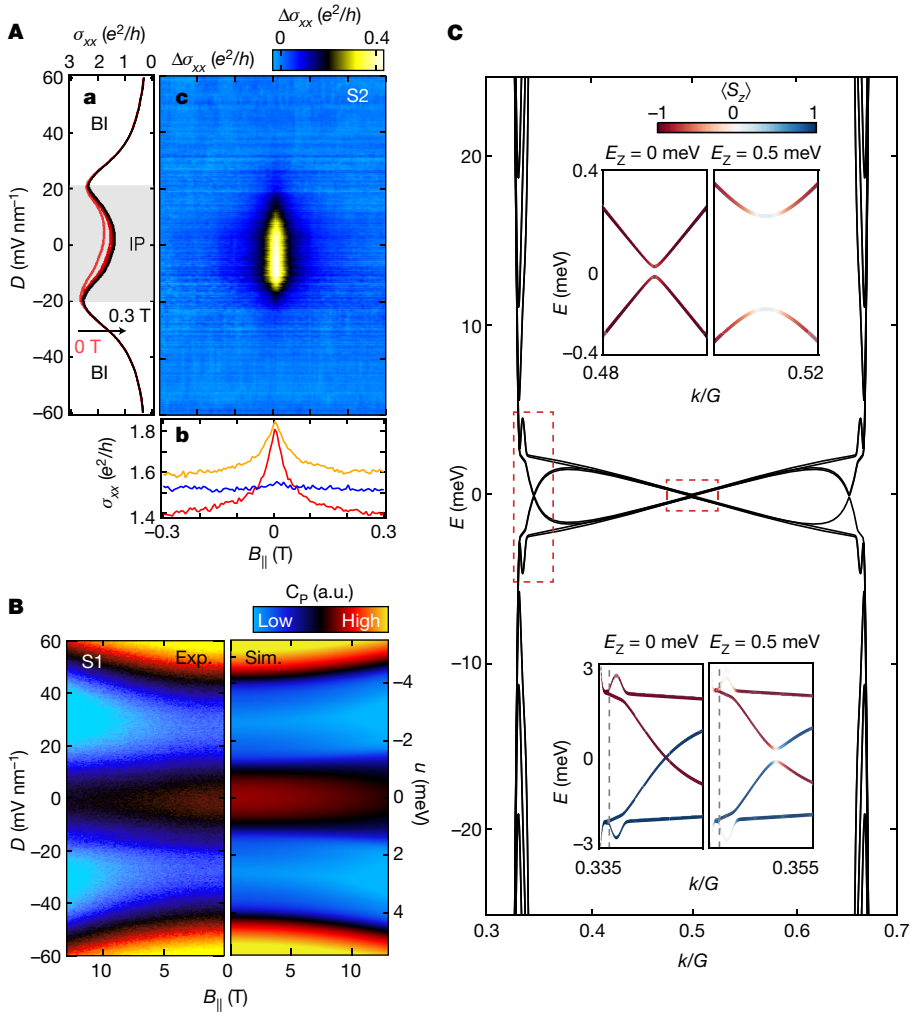

Fig. 3 | Magnetoconductance and edge state transport in the inverted phase. A, Longitudinal conductance, $\sigma_{xx} = 1/R_{xx}$, measured in a four-terminal geometry at $n = 0$. **a**, σ_{xx} as a function of D for different values of $B_\parallel$. The inverted phase (IP) is visible as a conductance suppression between $|D| < 20$ meV nm^{-1}, separated by conductance maxima from the band insulators (BIs) at large $|D|$. **b**, σ_{xx} as a function of $B_\parallel$ for different values of D (in mV nm^{-1}: red, 0; yellow, 10; blue, 30). Strong in-plane magnetoconductance is observed only in the inverted phase, and not in the band insulators. **c**, Subtracted $\Delta\sigma_{xx} = \sigma_{xx}(B_\parallel) - \sigma_{xx}(B_\parallel = 300\ \text{mT})$, highlighting that the anomalous in-plane magnetoconductance is restricted to the inverted phase. **B**, C_P as a function of D and $B_\parallel$ with $B_\perp = 0$ T. Experimental (Exp.) data for device S1 is plotted on the left and simulated (Sim.) C_P from the continuum model is plotted on the right. **C**, Band structure calculated for a 1,000-lattice-site-wide BLG ribbon with Ising SOC of equal magnitude ($\lambda_I = 5$ meV) and opposite sign on the opposite layers. Within the bulk gap, a set of spin-polarized energy bands emerge with wavefunctions tightly localized on the sample boundary. Top inset, detailed view of the edge states that approach $E = 0$ near the M point, corresponding to the dashed box on the left of the main panel, of the Brillouin zone for $E_Z = g\mu_B B_\parallel = 0$ (left) and $E_Z = 0.5$ meV (right). These states are not gapless even for $E_Z = \lambda_R = 0$. Bottom inset, the same calculations for edge states near the K point, corresponding to the dashed box at the centre of the main panel. While gapless for $E_Z = \lambda_R = 0$, in-plane field produces a gap proportional to E_Z.

The inverted phase is readily evident in resistance measurements of a symmetric device (S2, see Fig. 3A, a and Extended Data Fig. 9b), but is not a strong insulator, showing a finite four-terminal conductivity $\sigma_{xx} \gtrsim e^2/h$ at low temperatures. This is consistent with edge states with a finite transmission coefficient, as might be expected for a finite-length helical edge in which backscattering is suppressed but not completely forbidden. However, it is also consistent with bulk conduction through a mesoscopically disordered sample. We discriminate between these two scenarios using the response of σ_{xx} to a small in-plane magnetic field, $B_\parallel$, which breaks s_z conservation. $B_\parallel$ is expected to localize spin-filtered edge states rapidly while having a minimal effect on the bulk energy spectrum when $E_Z < \lambda_I$ (that is, $B_\parallel < 10$–20 T for $\lambda_I \approx 1$–2 meV). Indeed, the inverted phase shows strong in-plane magnetoresistance at exceptionally small values of $B_\parallel$, as shown in Fig. 3A, a–c: this response is completely absent in the band insulator phases. This is in contrast with C_P measurements of the bulk, which show no detectable dependence on $B_\parallel$ at low fields and a high-field response that is well accounted for in our theoretical model (Fig. 3B).

Numerical simulations of the band structure for a finite-width BLG ribbon (see Supplementary Information) are shown in Fig. 3C. In addition to the bulk gap, consistent with the continuum model, energy spectra additionally feature states localized on the edge of the ribbon that approach $E = 0$ at the K, K′ and M points in the Brillouin zone. Whereas the M point (Fig. 3C, top inset) edge states are gapped even in the absence of Rashba SOC, the states near the K and K′ points (Fig. 3C, bottom inset) are indeed gapless and helical. Simulations[22] show that the helical edge states are remarkably robust to Rashba SOC: the edge gap is strongly suppressed by interlayer hopping terms in the BLG band structure, so that the anticipated gap is $\Delta_{edge} \propto \lambda_R^2/\gamma_1 \approx 0.25$meV, where γ_1 is the interlayer hopping energy, even for $\lambda_R = 10$ meV, near the largest values reported in the literature[11]. In contrast, the helical edge states are sensitive to finite $B_\parallel$ (Fig. 3C, right panels of top and bottom insets), developing an energy gap directly proportional to the Zeeman energy, $\Delta_{edge} \approx g\mu_B B_\parallel \approx 0.1$ meV $\times B_\parallel$ (where $B_\parallel$ is in units of tesla).

These considerations are qualitatively consistent with the observed in-plane magnetoresistance anomaly. However, we note that the fine

structure of the edge states is highly sensitive to choice of theoretical parameters, and ignores electron–electron interactions, which may play an important role. Our experimental magnetoresistance data saturate at a rather low resistance value, well below h/e^2, possibly indicating residual bulk conductance. It bears noting that the weak edge transport is understood to be a consequence of the accidental approximate s_z-conservation in this system. However, recent theoretical work[22] argues that the same fabrication technique implemented with ABC trilayer graphene—where the induced SOC would gap a cubic band having a 3π Berry phase—results in a strong topological insulator with time-reversal symmetry protected edge states. Notably, the multi-layer graphene/WSe_2 platform generically allows for gate-tunable transitions between topological and trivial insulating states, which is a long-standing milestone in the quest for reconfigurable topological circuits.

Online content

Any Methods, including any statements of data availability and Nature Research reporting summaries, along with any additional references and Source Data files, are available in the online version of the paper at https://doi.org/10.1038/s41586-019-1304-2.

Received: 8 January 2019; Accepted: 5 April 2019;
Published online 12 June 2019.

1. Hasan, M. Z. & Kane, C. L. Colloquium: topological insulators. *Rev. Mod. Phys.* **82**, 3045–3067 (2010).
2. Qi, X.-L. & Zhang, S.-C. Topological insulators and superconductors. *Rev. Mod. Phys.* **83**, 1057–1110 (2011).
3. Kane, C. L. & Mele, E. J. Quantum spin Hall effect in graphene. *Phys. Rev. Lett.* **95**, 226801 (2005).
4. Min, H. et al. Intrinsic and Rashba spin-orbit interactions in graphene sheets. *Phys. Rev. B* **74**, 165310 (2006).
5. Huertas-Hernando, D., Guinea, F. & Brataas, A. Spin-orbit coupling in curved graphene, fullerenes, nanotubes, and nanotube caps. *Phys. Rev. B* **74**, 155426 (2006).
6. Yao, Y., Ye, F., Qi, X.-L., Zhang, S.-C. & Fang, Z. Spin-orbit gap of graphene: first-principles calculations. *Phys. Rev. B* **75**, 041401(R) (2007).
7. Sichau, J. et al. Resonance microwave measurements of an intrinsic spin-orbit coupling gap in graphene: a possible indication of a topological state. *Phys. Rev. Lett.* **122**, 046403 (2019).
8. Gmitra, M. & Fabian, J. Graphene on transition-metal dichalcogenides: a platform for proximity spin-orbit physics and optospintronics. *Phys. Rev. B* **92**, 155403 (2015).
9. Gmitra, M. & Fabian, J. Proximity effects in bilayer graphene on monolayer WSe_2: field-effect spin valley locking, spin-orbit valve, and spin transistor. *Phys. Rev. Lett.* **119**, 146401 (2017).
10. Wang, Z. et al. Strong interface-induced spin–orbit interaction in graphene on WS_2. *Nat. Commun.* **6**, 8339 (2015).
11. Wang, Z. et al. Origin and magnitude of 'designer' spin-orbit interaction in graphene on semiconducting transition metal dichalcogenides. *Phys. Rev. X* **6**, 041020 (2016).
12. Yang, B. et al. Tunable spin-orbit coupling and symmetry-protected edge states in graphene/WS_2. *2D Mater.* **3**, 031012 (2016).
13. Yang, B. et al. Strong electron-hole symmetric Rashba spin-orbit coupling in graphene/monolayer transition metal dichalcogenide heterostructures. *Phys. Rev. B* **96**, 041409 (2017).
14. Völkl, T. et al. Magnetotransport in heterostructures of transition metal dichalcogenides and graphene. *Phys. Rev. B* **96**, 125405 (2017).
15. Wakamura, T. et al. Strong anisotropic spin-orbit interaction induced in graphene by monolayer WS_2. *Phys. Rev. Lett.* **120**, 106802 (2018).
16. Zihlmann, S. et al. Large spin relaxation anisotropy and valley-Zeeman spin-orbit coupling in WSe_2/graphene/h-BN heterostructures. *Phys. Rev. B* **97**, 075434 (2018).
17. Avsar, A. et al. Spin-orbit proximity effect in graphene. *Nat. Commun.* **5**, 4875 (2014).
18. Dankert, A. & Dash, S. P. Electrical gate control of spin current in van der Waals heterostructures at room temperature. *Nat. Commun.* **8**, 16093 (2017).
19. Ghiasi, T. S. et al. Large proximity-induced spin lifetime anisotropy in transition-metal dichalcogenide/graphene heterostructures. *Nano Lett.* **17**, 7528–7532 (2017).
20. Omar, S. & van Wees, B. J. Spin transport in high-mobility graphene on WS_2 substrate with electric-field tunable proximity spin-orbit interaction. *Phys. Rev. B* **97**, 045414 (2018).
21. Benítez, L. A. et al. Strongly anisotropic spin relaxation in graphene–transition metal dichalcogenide heterostructures at room temperature. *Nat. Phys.* **14**, 303–308 (2018).
22. Zaletel, M. P. & Khoo, J. K. The gate-tunable strong and fragile topology of multilayer-graphene on a transition metal dichalcogenide. Preprint at https://arXiv.org/abs/1901.01294 (2019).
23. Gmitra, M., Kochan, D., Hogl, P. & Fabian, J. Trivial and inverted Dirac bands and the emergence of quantum spin Hall states in graphene on transition-metal dichalcogenides. *Phys. Rev. B* **93**, 155104 (2016).
24. Dean, C. R. et al. Boron nitride substrates for high-quality graphene electronics. *Nat. Nanotechnol.* **5**, 722–726 (2010).
25. Zibrov, A. A. et al. Tunable interacting composite fermion phases in a half-filled bilayer-graphene Landau level. *Nature* **549**, 360–364 (2017).
26. McCann, E. & Fal'ko, V. I. Landau-level degeneracy and quantum Hall Effect in a graphite bilayer. *Phys. Rev. Lett.* **96**, 086805 (2006).
27. Khoo, J. Y. & Levitov, L. Tunable quantum Hall edge conduction in bilayer graphene through spin-orbit interaction. *Phys. Rev. B* **98**, 115307 (2018).
28. Hunt, B. M. et al. Direct measurement of discrete valley and orbital quantum numbers in bilayer graphene. *Nat. Commun.* **8**, 948 (2017).
29. Garcia, J. H., Vila, M., Cummings, A. W. & Roche, S. Spin transport in graphene/transition metal dichalcogenide heterostructures. *Chem. Soc. Rev.* **47**, 3359–3379 (2018).

Acknowledgements Experimental work at UCSB was supported by the ARO under award MURI W911NF-16-1-0361. D.R. and J.C.H. acknowledge support by the US Department of Energy, DE-SC0016703, for synthesis of WSe_2 crystals. K.W. and T.T. acknowledge support from the Elemental Strategy Initiative conducted by the MEXT, Japan, and the CREST (JPMJCR15F3), JST. M.P.Z. was supported by the Director, Office of Science, Office of Basic Energy Sciences, Materials Sciences and Engineering Division of the US Department of Energy under contract no. DE-AC02-05-CH11231 (van der Waals heterostructures programme, KCWF16). A.F.Y. acknowledges the support of the David and Lucile Packard Foundation and the Alfred. P. Sloan Foundation. J.O.I. acknowledges the support of the Netherlands Organization for Scientific Research (NWO) through the Rubicon grant, project number 680-50-1525/2474. C.L. and L.S.L. acknowledge support of the STC Center for Integrated Quantum Materials under NSF grant no. DMR-1231319. J.Y.K. acknowledges support by the National Science Scholarship from the Agency for Science, Technology and Research (A*STAR). A portion of this work was performed at the National High Magnetic Field Laboratory, which is supported by National Science Foundation Cooperative Agreement no. DMR-1644779 and the State of Florida. Measurements made use of a dilution refrigerator funded through the Major Research Instrumentation Program of the US National Science Foundation under award no. DMR-1531389, and the MRL Shared Experimental Facilities, which are supported by the MRSEC Program of the US National Science Foundation under award no. DMR-1720256.

Reviewer information *Nature* thanks Saroj Prasad Dash and the other anonymous reviewer(s) for their contribution to the peer review of this work.

Author contributions J.O.I., X.C. and H.Z. fabricated the devices. J.O.I., X.C., E.M.S. and A.F.Y. performed the measurements. J.Y.K., C.L. and M.P.Z. performed the theoretical simulations, with J.Y.K. and C.L. advised by L.S.L. J.O.I., X.C., J.Y.K., C.L., L.S.L., M.P.Z. and A.F.Y. analysed the data. D.R. and J.C.H. grew the WSe_2 crystals used in devices A1, S1 and A2/S2. T.T. and K.W. grew the hBN crystals used in all devices. J.O.I. and A.F.Y. wrote the paper in consultation with X.C., J.Y.K., C.L., L.S.L. and M.P.Z.

Competing interests The authors declare no competing interests.

Additional information
Extended data is available for this paper at https://doi.org/10.1038/s41586-019-1304-2.
Supplementary information is available for this paper at https://doi.org/10.1038/s41586-019-1304-2.
Reprints and permissions information is available at http://www.nature.com/reprints.
Correspondence and requests for materials should be addressed to A.F.Y.
Publisher's note: Springer Nature remains neutral with regard to jurisdictional claims in published maps and institutional affiliations.

METHODS

Device fabrication and measurement. Five BLG van der Waals heterostructure devices (labelled C1, A1, S1, A2/S2, A3) were fabricated and studied in this work, as shown in Extended Data Fig. 1. All devices were fabricated using a stacking and transfer method based on van der Waals adhesion[30]. Contact to the BLG was achieved using approximately 10-nm-thick graphite flakes. All devices made use of single-crystal hBN gate dielectrics[24] and graphite gates[25], which in combination are known to minimize extrinsic charge disorder. Devices A1, S1 and A2/S2 were fabricated using WSe_2 crystals grown by a flux method[31], while device A3 was fabricated using WSe_2 from a commercial source (2Dsemiconductors.com). A mixture of CHF_3 and O_2 was used to dry etch the stacks to define the device area and create connections to the BLG and top and bottom gates. Electrical contact was made to the edges of the exposed graphite flakes using a three-layer metal film of Cr/Pd/Au (3 nm/15 nm/80 nm).

Penetration field capacitance measurements were performed on all devices and additional connections were patterned in device A2/S2 in order to perform electrical transport. With the exception of device A2/S2, all devices had characteristics corresponding to uniform encapsulation on each facet by either hBN or WSe_2, depending on the device configuration. Device A2/S2 showed two sets of LL phase transitions in the zero-energy LL, consistent with the device having one asymmetric portion (A2) and one symmetric portion (S2). Extended data from this device is presented in Extended Data Fig. 9.

Small changes in device capacitance are measured using a low-temperature capacitance bridge[32], which effectively disconnects the device capacitance from the large capacitance of the cryostat cabling, see Extended Data Fig. 2. C_P is a measure of the capacitance between the top and bottom gates, and its magnitude is high when the BLG is incompressible (gapped) and low when it is compressible (conducting). C_P is measured by applying a fixed a.c. excitation (17–33 kHz) to the top gate (δV_{top}), and the phase and amplitude of a second a.c. excitation with the same frequency is adjusted and applied to a standard reference capacitor (C_{ref}) on the low-temperature amplifier in order to balance the capacitance bridge. A commercial high-electron-mobility transistor (FHX35X) transforms the small sample impedance to a 1 kΩ output impedance roughly translating to a (power) gain of about 1,000. V_{top} (top-gate voltage) and V_{samp} (sample voltage) are swept at a fixed V_{gate} (gate voltage) in order to adjust charge density $n = c_t\nu_t + c_b\nu_b$ and displacement field $D = (c_t\nu_t - c_b\nu_b)/(2\epsilon_0)$.

All measurements were performed within the electronic bandgap of WSe_2. Charge accumulation in the WSe_2 layers is evident in capacitance measurements at high densities and manifests as apparent negative signals in C_P as charge carriers are transferred from BLG to the opposite facet of the WSe_2 substrates.

Data and simulations at $B = 0$ for varying λ_R. In order to determine what type of spin–orbit symmetry breaking terms are present in the symmetric device, we analyse the band structure and simulated capacitance C_P for a one-sided device in further detail. As discussed in the main text, the band structure and in turn the system for the symmetric device are almost completely insensitive to the value of the Rashba SOC under the assumption of equal and opposite Rashba coupling in the top and bottom layer. To circumvent this peculiar property we focus on the one-sided device, which does not exhibit similar insensitivity to Rashba SOC due to its asymmetric construction.

The measured capacitance for the one-sided device is shown in Extended Data Fig. 4a. In addition to the symmetric gapped regions due to the applied interlayer potential (as also seen in the control device, C1), we observe two clearly defined asymmetric features (indicated with white arrows in Extended Data Fig. 4a) present in the $D > 0$, $n > 0$ and $D < 0$, $n < 0$ regions. Each feature consists of line-like 'dips' in capacitance (see the linecut taken at the dashed line in Extended Data Fig. 4a plotted in Extended Data Fig. 4e). By definition, minima in C_P correspond to maxima of compressibility. A maximum of compressibility in turn suggests an extremum of the band structure (van Hove singularities). With this understanding in mind we consider three separate device simulations. (1) A pure Ising SOC system: non-zero Ising coupling, zero Rashba coupling (Extended Data Fig. 4b). (2) A pure Rashba SOC system: zero Ising coupling, non-zero Rashba coupling (Extended Data Fig. 4c). (3) A mixed system: non-zero Ising coupling, non-zero Rashba coupling (Extended Data Fig. 4d).

Corresponding band structures for the pure Ising (Extended Data Fig. 4i–l) and pure Rashba (Extended Data Fig. 4m–p) devices are shown in the panels below the capacitance simulations. We clearly see that neither a Rashba nor an Ising term leads to formation of a local minimum of the band structure. The Ising SOC together with interlayer potential causes an energy splitting of either conduction or valence bands (Extended Data Fig. 4i), while the Rashba SOC causes primarily splittings in momenta (Extended Data Fig. 4m). Of these two effects, only the splitting in energy will lead to two van Hove singularities, as seen in the experimental map in Extended Data Fig. 4a and the linecut in Extended Data Fig. 4e. The split band for electrons corresponds to the dips in experimental C_P and simulated C_P marked by the square and circle symbols in Extended Data Fig. 4a, b, e, f. The splitting is also evident in the calculated density of states (DOS) shown in Extended Data Fig. 4h with a linecut in Extended Data Fig. 4g. The two peaks in DOS for electrons correspond directly to the dips in C_P. The splitting is further exemplified by the energy contour plots of the two systems (Extended Data Fig. 4j–l and Extended Data Fig. 4n–o), which show a clear difference between band structures for the pure Ising and pure Rashba devices. We note however that a mixed system (both a non-zero Ising term and a non-zero Rashba term) cannot be excluded on the basis of this analysis as the capacitance of the mixed system possesses all qualitative features of a pure Ising device, as shown in Extended Data Fig. 4d.

$\nu = \pm 3$ phase transitions in C1 and comparison with A1. The energy spectrum in BLG subjected to a quantizing perpendicular field is described by highly degenerate Landau levels (LLs). Two-fold quasi-degeneracies of the inequivalent valleys ($\xi = \pm 1$), spin projections ($s = \pm 1$), and the lowest two orbital ($N = 0, 1$) LLs[26] combine to form an octet LL spanning $\nu \in (-4, 4)$, where $\nu = 2\pi\ell_B^2 n$ denotes the LL filling factor. The degeneracy between individual octet sublevels $|\xi N s\rangle$ is lifted by small intrinsic level splittings that include the Zeeman effect (lifting the spin degeneracy), interlayer potential u (lifting the valley degeneracy through the near-perfect equivalence of valley and layer polarization in the lowest LLs[26]) and band structure effects that distinguish the two orbitals. If disorder is sufficiently low, these splittings tend to fully polarize the electron system into one or more of the $|\xi N s\rangle$, which manifests experimentally as incompressible phases at all integer ν. As shown in Fig. 2d, this signature is present in WSe_2 supported samples, which show signs of full lifting of the octet degeneracy for $B_\perp \gtrsim 2$ T.

In the control device, C1, we do not expect to observe a Zeeman dependence of $D^*_{\nu=\pm 3}$ as the transitions occur between states with the same spin orientation. Extended Data Fig. 5a shows the LL spectrum at $B = 5$ T for BLG without SOC. The level transitions at $u^*_{\nu=-3}$ are between $|-0\uparrow\rangle$ and $|+0\uparrow\rangle$. The applied magnetic field simply moves these two states down in energy, shifting the energy at which the transition occurs but keeping it pinned to $u = 0$ meV. This can be readily seen for C1 in the extracted D^* from measurements of C_P, see Extended Data Fig. 5b. D^* is constant across the measurable field range. Note that offsets from $u^* = 0$ are possible due to differing on-site energies within the BLG unit cell, which can arise from coupling to the hBN substrate, but that these offsets do not influence the spin degree of freedom. This is in contrast with the asymmetric device with a layer-specific SOC. Extended Data Fig. 5c shows the calculated LL spectrum for BLG now with an Ising SOC of $\lambda_I = 5$ meV. The level transitions for both $\nu = -3$ and $\nu = +3$ have been shifted away from $u = 0$ meV as a result of the rearrangement of the states on the bottom layer. Not only has the transition shifted from zero but the transitions now occur between states with opposite spin orientation. Application of a magnetic field acts to shift the levels in opposite directions, thereby changing the u^* at which the transition occurs. This is again readily observed in the data for an asymmetric device, A1, shown in Extended Data Fig. 5d. $D^*_{\nu=\pm 3}$ moves to lower D at larger magnetic fields. An illustration of the canting of the spin in the spin–orbit coupled layer in an asymmetric device is shown in Extended Data Fig. 8e. As the in-plane field is increased, the spin in the proximitized layer cants towards the total magnetic field vector.

Measurements at higher magnetic fields. At higher magnetic fields, we observe fractional quantum Hall and Chern insulator states that are a testament to the quality of the heterostructures even with the incorporation of WSe_2. Extended Data Fig. 6 shows C_P measurements of the zero-energy LL for devices C1 (Extended Data Fig. 6a), A1 (Extended Data Fig. 6b) and S1 (Extended Data Fig. 6c) taken at 18 T. In the control device, incompressible states are observed at integer and fractional fillings consistent with our previous findings[25]. Remarkably, the same is true for A1 and S1 where the same filling sequences are observed. The red dashed line in Extended Data Fig. 6c shows the location of the high-resolution C_P linecut shown in Extended Data Fig. 7a where fractional states are clearly observed. In device A3, fabricated with commercially obtained WSe_2, we observe fractional Chern insulator states at even higher fields[33]. Extended Data Fig. 7b shows C_P as a function of nominal charge density n_0/c, where c is the geometric capacitance, and $B_\perp$. Extended Data Fig. 7c shows a schematic of the insulating states observed in Extended Data Fig. 7b. Fractional Chern insulating states at 1/3, 2/5, 3/5 and 2/3 filling are observed within the Chern band defined between $(t, s) = (1, 1)$ and $(2, 0)$ (black lines), where t and s are classifiers for the insulating states, see ref. [33] for details.

Asymmetries in $\nu \neq \pm 3$ LL crossings. In addition to the crossing observed between LL coincidences for $\nu = \pm 3$ for device A1, we also observe similar crossings at the same critical magnetic field, defined by the strength of λ_I, for $\nu = \pm 1$ (Extended Data Fig. 8b) and $\nu = \pm 2$ (Extended Data Fig. 8c). While the dependence of these crossings on magnetic field is similar to the $\nu = \pm 3$ case, interactions become important for these level crossings and their full evolution is outside the scope of our single-particle theoretical model. The excited-state LLs ($N = \pm 2$; Extended Data Fig. 8d–f) and ($N = \pm 3$; Extended Data Fig. 8g–i)

additionally show strong asymmetries away from zero displacement field and nonlinear dependence on magnetic field presumably due to the proximity induced SOC.

Data from device A2/S2. Device A2/S2 (Fig. 3A and Extended Data Fig. 9) was fabricated with the intention of producing a symmetric device. However, capacitance measurements and post facto optical microscopy show a misalignment in one region (indicated in Extended Data Fig. 9a, resulting in a small area of the device in which only one facet of the BLG is in contact with WSe_2. Capacitance measurements, which are sensitive to areal averages of DOS, indeed detect twice the normal number of phase transitions (Extended Data Fig. 9d), which show features characteristic, respectively, of both symmetric and asymmetric devices S1 and A1. In particular, one set of phase transitions shows the characteristic crossing of the $D^*_{\nu\pm3}$ transitions in finite field, resulting in a measured $\lambda_I = 2.0$ meV (Extended Data Fig. 9e). Transport measurements are performed on the side of the device that is completely encapsulated: these show clearly the inverted phase at zero field (Extended Data Fig. 9b) and the high in-plane field response (Extended Data Fig. 9c), similar to that found in device S1 with magnetocapacitance measurements.

Data availability

The datasets generated during and/or analysed during the current study are available from the corresponding author on reasonable request.

30. Wang, L. et al. One-dimensional electrical contact to a two-dimensional material. *Science* **342**, 614–617 (2013).
31. Gustafsson, M. V. et al. Ambipolar Landau levels and strong band-selective carrier interactions in monolayer WSe_2. *Nat. Mater.* **17**, 411–415 (2018).
32. Ashoori, R. C. et al. Single-electron capacitance spectroscopy of discrete quantum levels. *Phys. Rev. Lett.* **68**, 3088–3091 (1992).
33. Spanton, E. M. et al. Observation of fractional Chern insulators in a van der Waals heterostructure. *Science* **360**, 62–66 (2018).

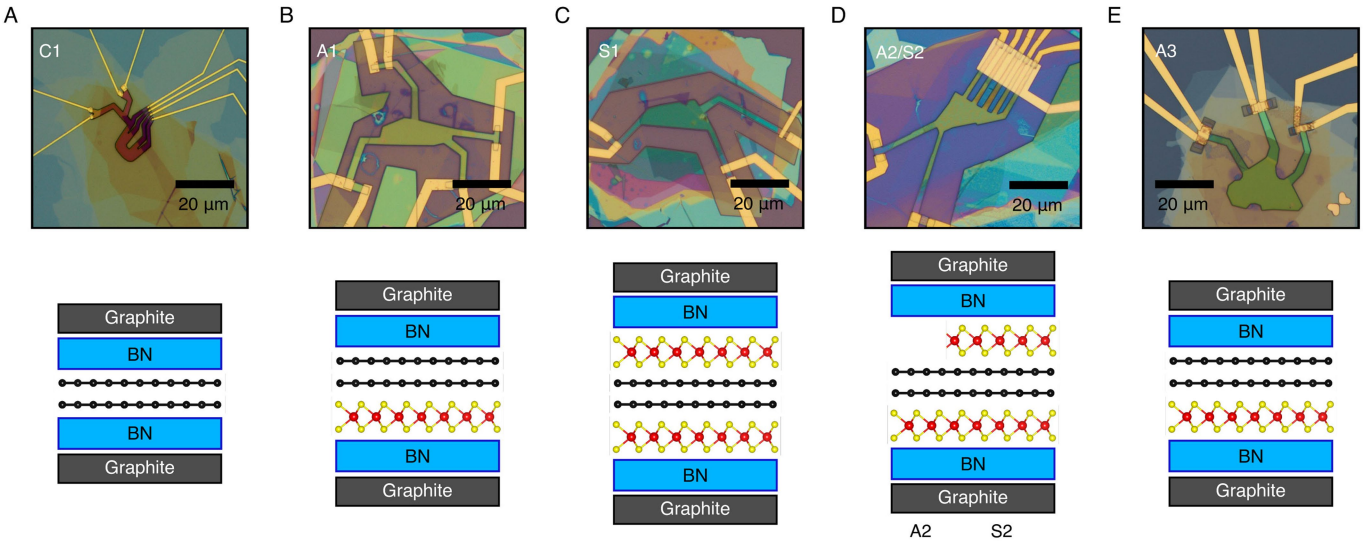

Extended Data Fig. 1 | Optical images and corresponding models for all the devices studied. For each device, the optical image is shown at the top and the corresponding model shown under. **a**, Control device C1. **b**, Asymmetric device A1. **c**, Symmetric device S1. **d**, Another symmetric device with a single-sided region. Details about this device are presented in Extended Data Fig. 9. **e**, Another asymmetric device, A3. This device showed additional features in the magnetocapacitance measurements that are associated with a moiré superlattice potential due to alignment of the BLG with the top hBN, see Extended Data Fig. 7.

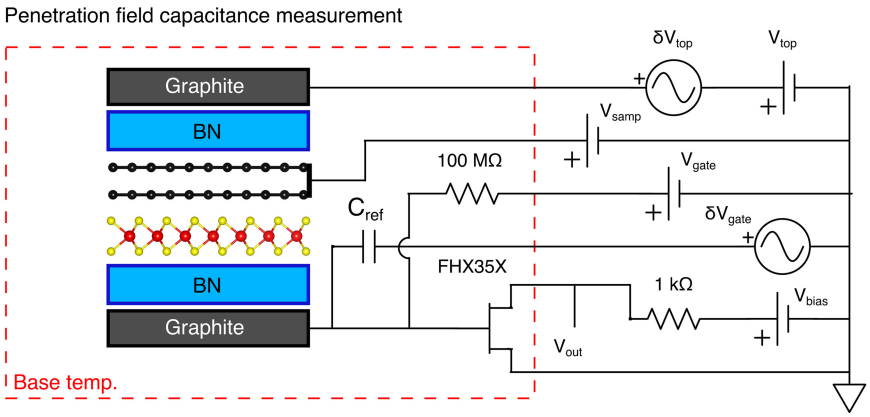

Extended Data Fig. 2 | Electrical schematic showing the details of the penetration field capacitance measurements. The components enclosed in the red dashed box are inside the cryostat, held at base temperature. Voltages are applied to V_{top} and V_{samp} (at a fixed V_{gate}) in order to adjust charge density $n = c_t v_t + c_b v_b$ and displacement field $D = (c_t v_t - c_b v_b)/(2\epsilon_0)$. See Methods for details.

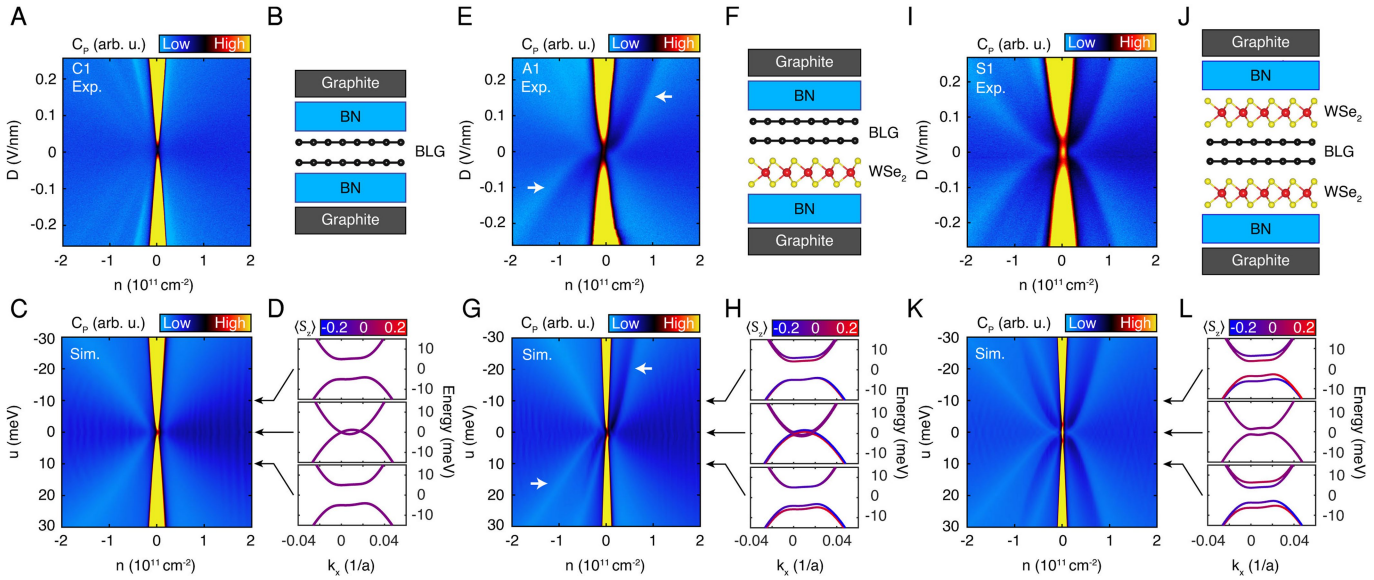

Extended Data Fig. 3 | Comparison between experimental and simulated penetration field capacitance for the three device configurations studied. a, Penetration field capacitance, C_P, as a function of charge density n and displacement field D measured at $B = 0$ and $T \approx 50$ mK in the control device, C1. **b**, Schematic of device C1, a BLG flake encapsulated with hBN. **c**, Simulated C_P as a function of interlayer bias, u, and charge density, n, from a low-energy continuum model for device C1. **d**, Low-energy bands for C1 near the K point of the Brillouin zone with $k_y = 0$. Line colour represents the expectation value of the out-of-plane projection of the electron spin, $\langle S_z \rangle$. Panels correspond to $u = -10$ meV (top), $u = 0$ meV (middle) and $u = 10$ meV (bottom). **e**, C_P for device A1. Arrows indicate weak features in C_P. **f**, Schematic of device A1, in which the BLG is asymmetrically encapsulated between WSe_2 and hBN crystals. **g**, Simulated C_P for the asymmetric geometry with $\lambda_I = 1.7$ meV Ising SOC on the bottom layer. Arrows denote band-edge singularity-associated features arising from spin-split valence (conduction) bands for electron (hole) doping, visible in **h**, the low-energy band structure. **h**, Low-energy bands for A1 near the K point of the Brillouin zone with $k_y = 0$. Line colour represents the expectation value of the out-of-plane projection of the electron spin, $\langle S_z \rangle$. Panels correspond to $u = -10$ meV (top), $u = 0$ meV (middle), and $u = 10$ meV (bottom). **i**, C_P measured for device S1. Note the incompressible phase centred at $D = 0$, $n = 0$, absent in either control or symmetric devices. **j**, Schematic of device S1, in which the BLG is symmetrically encapsulated between two few-layer WSe_2 crystals. **k**, Simulated C_P for the symmetric geometry, with an Ising SOC of equal magnitude ($\lambda_I = 2.6$ meV) but opposite signs on opposite layers. **l**, Low-energy bands for S1 in the symmetric geometry near the K point of the Brillouin zone with $k_y = 0$. Line colour represents the expectation value of the out-of-plane projection of the electron spin, $\langle S_z \rangle$. Panels correspond to $u = -10$ meV (top), $u = 0$ meV (middle), and $u = 10$ meV (bottom).

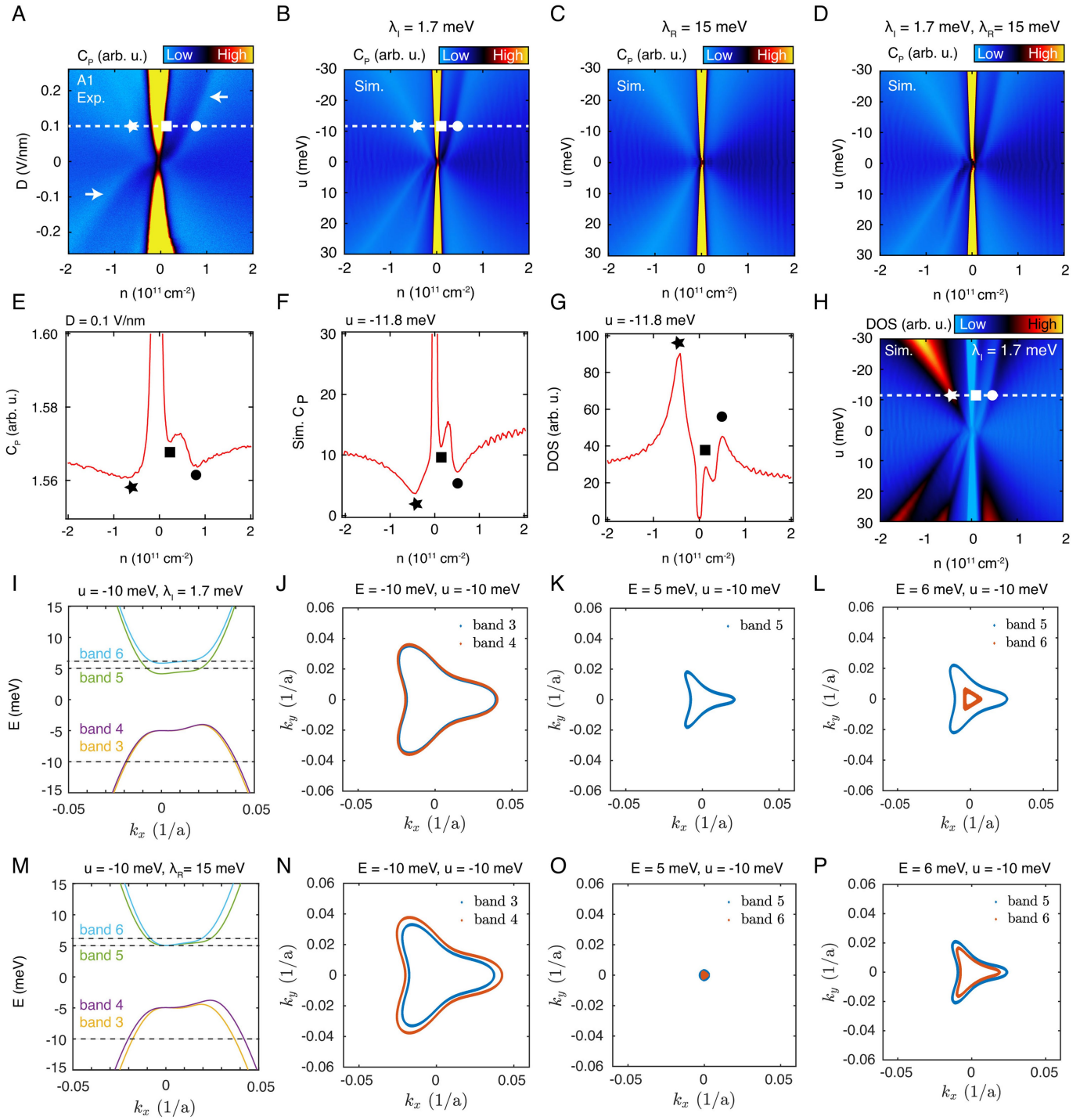

Extended Data Fig. 4 | Comparison between experimental data and numerical simulations including λ_I and λ_R. a, Measured C_P of device A1 as a function of n and D. **b–d**, Simulated C_P from a low-energy continuum model with SOC as follows: **b**, a one-sided Ising SOC of $\lambda_I = 1.7$ meV; **c**, a one-sided Rashba SOC of $\lambda_R = 15$ meV; and **d**, a one-sided Ising SOC of $\lambda_I = 1.7$ meV and a Rashba SOC of $\lambda_R = 15$ meV. **e**, Linecut taken at the location of the dashed white line ($D = 0.1$ V nm^{-1}) in **a**. The symbols mark dips in C_P indicated with the same symbols in **a**. **f**, Linecut of the simulated data in **b** taken at $u = -11.8$ meV, equivalent to a displacement field of 0.1 V nm^{-1} for device A1. The symbols mark dips in C_P indicated with the same symbols in **b**. **g**, Linecut of the calculated density of states (DOS) in **h** for device A1 taken at $u = -11.8$ meV, equivalent to a displacement field of 0.1 V nm^{-1} for device A1. The symbols mark peaks in DOS which correspond to dips in C_P indicated with the same symbols in **a**, **b**, **e**, **f** and **g**. **h**, Calculated DOS for device A1. **i**, Low-energy bands (specifically bands 3–6) near the K point of the Brillouin zone with $k_y = 0$, $u = -10$ meV and $\lambda_I = 1.7$ meV. A clear band splitting is observed in the conduction band associated with the addition of an Ising SOC. **j–l**, Fermi contours at $E = -10$ meV and $u = -10$ meV (**j**), $E = 5$ meV and $u = -10$ meV (**k**), and $E = 6$ meV and $u = -10$ meV (**l**). **m**, Low-energy bands near the K point of the Brillouin zone with $k_y = 0$, $u = -10$ meV and $\lambda_R = 15$ meV. **n–p**, Fermi contours at $E = -10$ meV and $u = -10$ meV (**n**), $E = 5$ meV and $u = -10$ meV (**o**) and $E = 6$ meV and $u = -10$ meV (**p**).

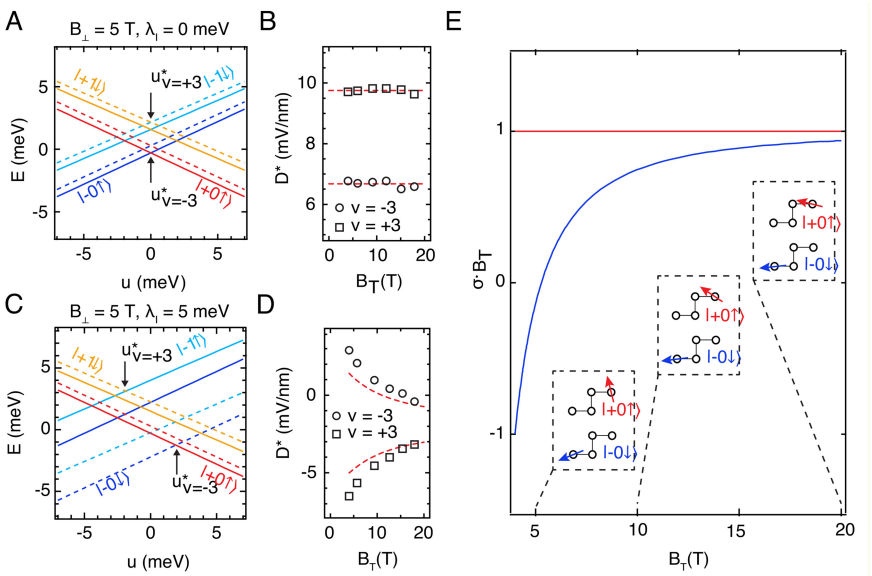

Extended Data Fig. 5 | Comparison between the $\nu = \pm 3$ phase transitions in the control device C1 and the asymmetric device A1. **a**, Energy level diagram of the zero-energy LL in the absence of SOC. The $\nu = \pm 3$ transitions are occurring between ground states with identical spin polarization. Note that offsets from $u^* = 0$ are possible due to differing on-site energies within the BLG unit cell, which can arise from coupling to the hBN substrate, but that these offsets do not influence the spin degree of freedom. The solid and dashed lines differentiate spin orientation. **b**, Measured $D^*_{\nu=\pm 3}$ as a function of the total magnetic field (B_T) for fixed $B_\perp = 4$ T in control device C1. No Zeeman dependence is observed, consistent with expectations from an SOC-free model. The red dashed line is the average value of $D^*_{\nu=\pm 3}$. **c**, Energy level diagram of the zero-energy LL with a layer-selective Ising SOC of $\lambda_I = 5$ meV, with sign chosen so that the effect of the SOC opposes the external field (reproduced from Fig. 2f of the main text). Note that the $\nu = \pm 3$ transitions now occur between ground states with opposite spin polarization. **d**, Measured $D^*_{\nu=\pm 3}$ as a function of B_T for fixed $B_\perp = 4$ T in device A1, reproduced from the main text. The red dashed line is a two-parameter fit with $\lambda_I = 1.7$ meV and $\epsilon_{BLG} = 2.8$, with the latter needed for the conversion between experimentally measured D and theoretically calculated u. **e**, Schematic of the effect of B_T in an asymmetric device. The red curve plots the dot product of the spin orientation on the top layer and the magnetic field, and the blue curve plots the product of the spin orientation on the bottom layer and the magnetic field. Whereas the LL in the unaffected layer always aligns its spin polarization with the external magnetic field (see the red arrows in the dashed boxes for total external magnetic fields of 5, 10 and 20 T, respectively), the spin polarization of LLs in the SOC-proximitized bottom layer result from a competition between SOC-induced Zeeman field (out of plane) and the changing direction of the physical Zeeman field (see the blue arrows in the dashed boxes). The affected spin cants only slightly for $E_Z \ll \lambda_I$, but eventually the Zeeman energy overwhelms the SOC and the two spins align as $E_Z/\lambda_I \to \infty$.

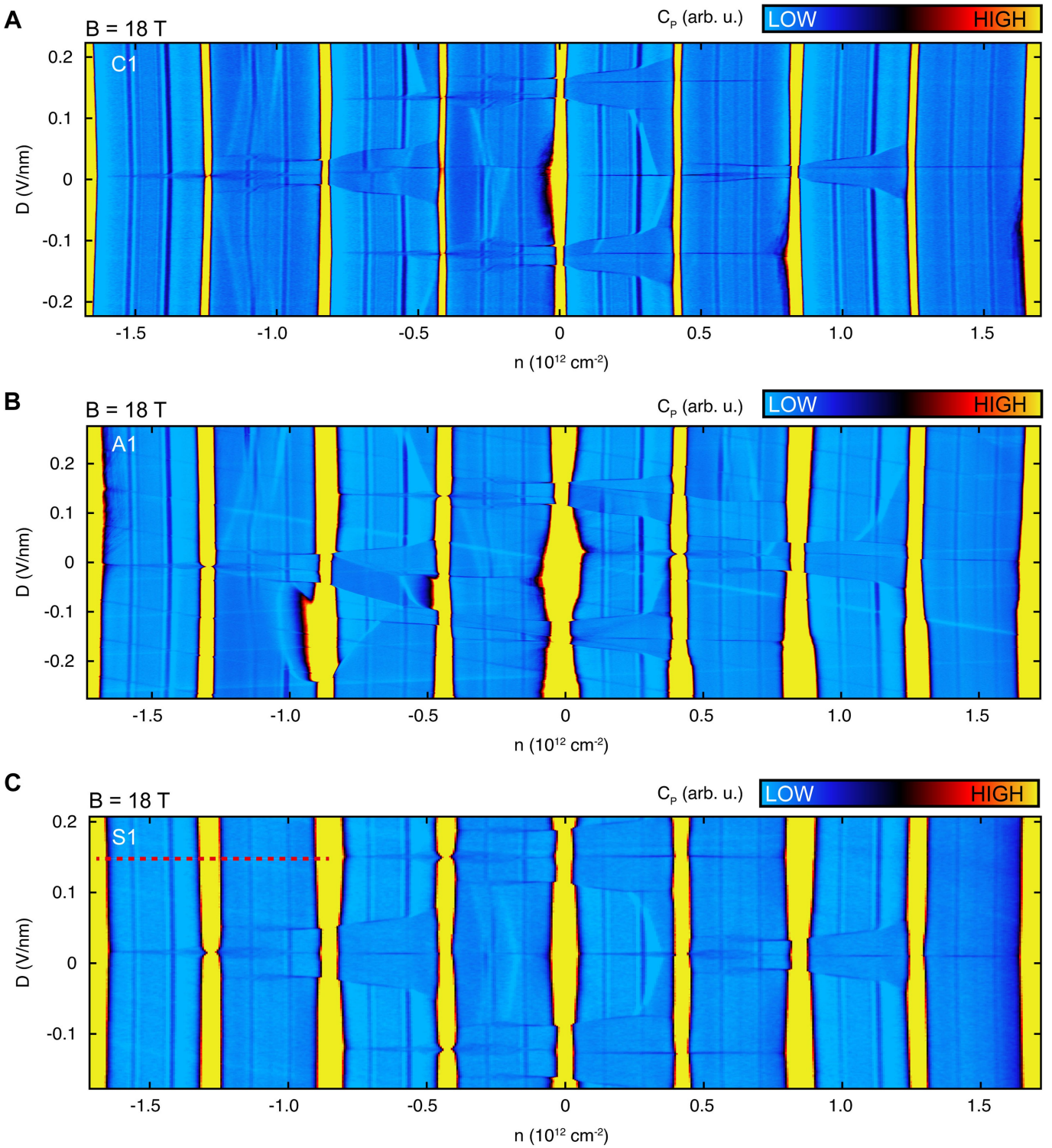

Extended Data Fig. 6 | Measured penetration field capacitance for devices A1, C1 and S1 at 18 T. a–c, C_P measured as a function of D and n at $B = 18$ T for devices C1 (**a**), A1 (**b**) and S1 (**c**). The red dashed line in c shows the location of the linecut plotted in Extended Data Fig. 7a.

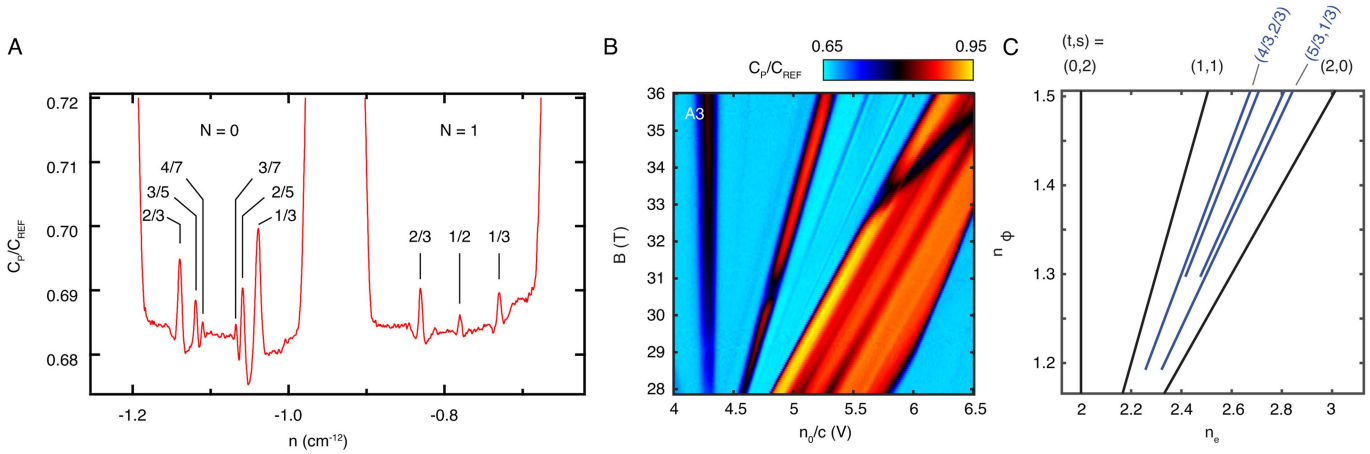

Extended Data Fig. 7 | Fractional quantum Hall and Chern insulator states at high magnetic field. a, Fractional quantum Hall states (black labels) observed at 18 T in device S1. C_P/C_{ref} taken at $D = 1.5$ V nm^{-1} in Extended Data Fig. 6c (red dashed line), corresponding to a range of $-4 < \nu < -2$. In the $N = 0$ orbital, fractional quantum Hall states up to sevenths are clearly observed. In the $N = 1$ orbital, an incompressible state is observed at half-filling. **b**, Fractional Chern insulator states in asymmetric device A3 at high magnetic fields with the BLG and hBN perfectly aligned. C_P (normalized by C_{ref}) is shown as a function of nominal electron density n_0/c (where c is the geometric capacitance) and applied perpendicular magnetic field B, at a fixed polarizing electric field $p_0\left(\frac{p_0}{c} = \frac{2\epsilon_0}{c}D = -6\text{V}\right)$. **c**, Schematic of the observed insulating states in units normalized to the moiré unit cell area ($A_{\text{moiré}}$): these are the number of flux quanta per moiré unit cell n_Φ ($= B/A_{\text{moiré}}\Phi_0$) and the number of electrons per moiré unit cell $n_e = n/A_{\text{moiré}}$, where $\Phi_0 = h/e$ is a flux quantum and n is the electron density. The insulating states are characterized by their inverse slope and intercept in these units, t and s, respectively. We observe a topological Chern band with $\delta t = C = 1$ and $\delta s = 1$, which originates at $n_\Phi = 1$ between insulating states $(t, s) = (1, 1)$ and $(2, 0)$ (black lines). We observe fractional Chern insulating states at 1/3, 2/5, 3/5, 2/3 filling of the band (blue lines) with quantum numbers $t, s = (4/3, 2/3), (7/5, 3/5), (8/5, 2/5), (5/3, 1/3)$, labelled respectively.

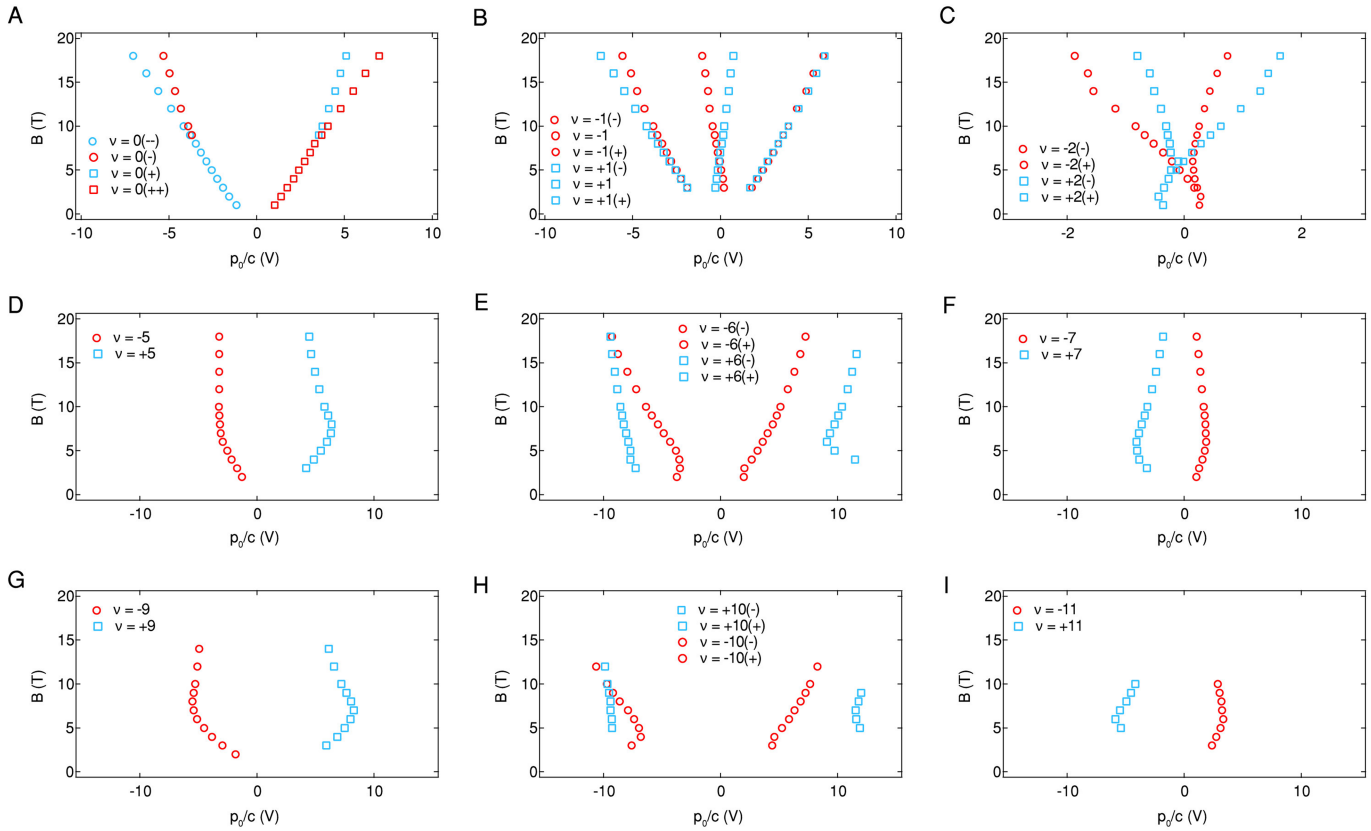

Extended Data Fig. 8 | Phase transitions as a function of magnetic field for the rest of the zeroth LL and the $N = 2$, 3 excited states. Following the analysis for $D^*_{\nu=\pm3}$ in Fig. 2h, we plot the dips in C_P at corresponding polarizations ($p_0/c \propto D$) as a function of perpendicular magnetic field (B) in device A1 for $\nu = 0$ (**a**), $\nu = \pm1$ (**b**), $\nu = \pm2$ (**c**), $\nu = \pm5$ (**d**), $\nu = \pm6$ (**e**), $\nu = \pm7$ (**f**), $\nu = \pm9$ (**g**), $\nu = \pm10$ (**h**) and $\nu = \pm11$ (**i**). The labels $(-, +)$ indicate the different phase transitions for each integer gap.

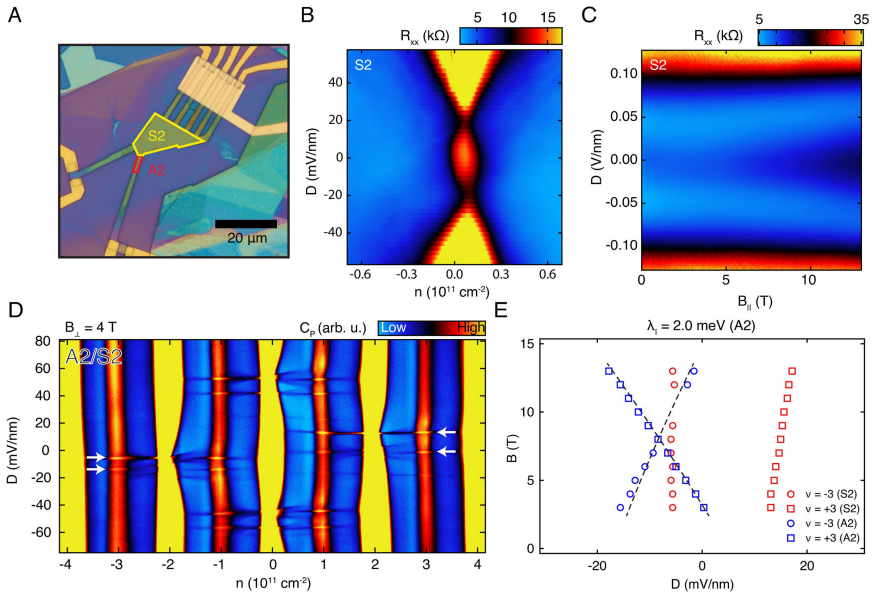

Extended Data Fig. 9 | Summary of data from device A2/S2. a, Optical image of device A2/S2. **b**, R_{xx} as a function of D and n at $B = 0$ T for the S2 portion of the device. The inverted phase is evident at charge neutrality and zero displacement field. **c**, R_{xx} as a function of $B_{\|}$ and D for the S2 portion. **d**, C_P as a function of n and D at $B = 4$ T for device A2/S2. Two sets of $\nu = \pm 3$ transitions are evident, indicated by the white arrows. **e**, $\nu = \pm 3$ transitions for device A2/S2. The crossing between $\nu = -3$ and $\nu = +3$ coming from the one-sided portion of the device (A2) is consistent with the crossing found in the asymmetric device A1. No crossing is evident in the symmetric portion which is consistent with transitions in S1.